Focus Section: Data Mine: 2019 Ridgecrest, California Earthquake Sequence

Coseismic Displacements and Surface Fractures from Sentinel-1 InSAR: 2019 Ridgecrest Earthquakes

Xiaohua Xu*[1], David T. Sandwell[1], and Bridget Smith-Konter[2]

Abstract

Interferometric Synthetic Aperture Radar is an important tool for imaging surface deformation from large continental earthquakes. Here, we present maps of coseismic displacement and strain from the 2019 Ridgecrest earthquakes using multiple Sentinel-1 images. We provide three types of interferometric products. (1) Standard interferograms from two look directions provide an overview of the deformation and can be used for modeling coseismic slip. (2) Phase gradient maps from stacks of coseismic interferograms provide high-resolution (~30 m) images of strain concentration and surface fracturing that can be used to guide field surveys. (3) High-pass filtered, stacked, unwrapped phase is decomposed into east–west and up–down, south–north components and is used to determine the sense of fault slip. The resulting phase gradient maps reveal over 300 surface fractures, including triggered slip on the Garlock fault. The east–west component of high-pass filtered phase reveals the polarity of the strike-slip offset (right lateral or left lateral) for many of the fractures. We find a small number of fractures that have slip polarity that is retrograde to the background tectonic stress. This is similar to observations of retrograde slip observed near the 1999 M_w 7.1 Hector Mine rupture, but the Ridgecrest observations are more completely imaged by the frequent and high-quality acquisitions from the twin Sentinel-1 spacecrafts. Determining whether the retrograde features are triggered slip on existing faults, or compliant fault deformation in response to stress changes from the Ridgecrest earthquakes, or new Coulomb-style failures, will require additional field work, modeling, and analysis.

Cite this article as Xu, X., D. T. Sandwell, and B. Smith-Konter (2020). Coseismic Displacements and Surface Fractures from Sentinel-1 InSAR: 2019 Ridgecrest Earthquakes, *Seismol. Res. Lett.* **XX**, 1–7, doi: 10.1785/0220190275.

Introduction

The M_w 7.1 Ridgecrest earthquake struck on 5 July 2019 at 8.19 p.m. local time at the China Lake Naval Air Center, 17 km northeast of the city of Ridgecrest, California (U.S. Geological Survey [USGS], 2019a). Thirty-six hours prior, on 4 July 2019, an M_w 6.4 foreshock occurred (10.33 a.m. local time), 11 km southwest of Searles Valley (USGS, 2019b). The two earthquakes ruptured two conjugate faults in the Airport Lake fault zone and Little Lake fault zone, oriented roughly northwest–southeast (right-lateral strike slip) and northeast–southwest (left-lateral strike slip), respectively. Field scientists reported 2–3 m of right-lateral offset along the southern section of the M_w 7.1 rupture.

Twin Sentinel-1 satellites operated by the European Space Agency (ESA) were continuously collecting measurements over this region since 2015 (Torres *et al.*, 2012). These satellites collect wide swath data (250 km) using a burst acquisition mode called terrain observation by progressive scan (TOPS). The twin satellites achieve complete coverage in a short-time interval of six days that is well suited for this earthquake sequence. The new wide swath mode requires along-track alignment of better than 1/200 of a pixel (<7 cm), which is possible using the very accurate orbital information provided by ESA (Sansosti *et al.*, 2006; Xu *et al.*, 2017); earthquake displacements greater than ~7 cm in the along-track direction will cause phase discontinuities at burst boundaries that should be ignored in the interpretation of the maps in the following sections. Moreover, the Sentinel-1 coverage is excellent for these two earthquakes, providing critical high resolution spatially dense deformation observations of the largest earthquake to strike the Eastern California Shear Zone (ECSZ) in nearly 20 yr (Fig. 1). In this article, we focus on mapping coseismic displacement and strain with the objective of serving these products to the field mapping and modeling communities

1. Institute of Geophysics and Planetary Physics, Scripps Institution of Oceanography, University of California San Diego, La Jolla, California, U.S.A.; 2. Department of Geology and Geophysics, University of Hawaii at Manoa, Honolulu, Hawaii, U.S.A.

*Corresponding author: xix016@ucsd.edu

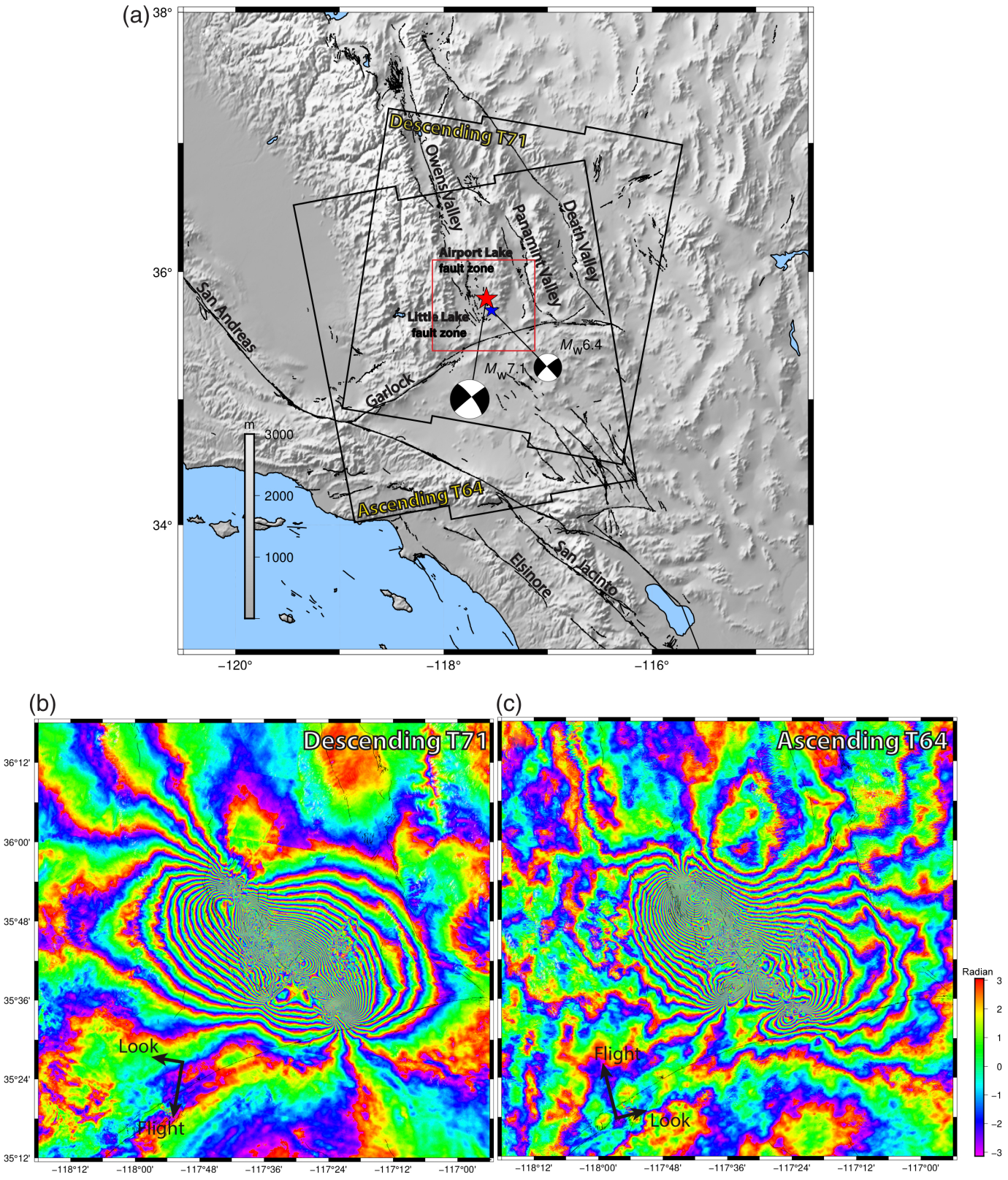

Figure 1. (a) Overview map of the topography, faults, and Sentinel-1 frames surrounding the 2019 Ridgecrest earthquake sequence. Red and blue stars denote the epicenter of the M_w 7.1 and 6.4 earthquakes, respectively. Black curves are faults mapped by U.S. Geological Survey (USGS). Red box indicates geographic location of the wrapped interferogram maps provided in (b) and (c). (b) Interferogram from the descending track 71 Sentinel-1 Interferometric Synthetic Aperture Radar (InSAR) data. Each fringe represents 2.8 cm of ground displacement away from the satellite. (c) Interferogram from the ascending track 64 Sentinel-1 InSAR data. The color version of this figure is available only in the electronic edition.

TABLE 1
Interferometric Pairs versus Perpendicular Baseline

Direction	Dates (yyyy/mm/dd)	$B_\perp$ (m)
Descending average look vector: [0.633, –0.112, 0.765]	2019/06/22–2019/07/16	87.79
	2019/06/22–2019/07/28	38.09
	2019/07/04–2019/07/16 (Fig. 1b)	29.68
	2019/07/04–2019/07/28	31.15
Ascending average look vector: [–0.636, –0.112, 0.763]	2019/06/28–2019/07/10	63.38
	2019/06/28–2019/07/16	35.98
	2019/06/28–2019/07/22	12.37
	2019/06/28–2019/07/28	25.96
	2019/06/28–2019/08/03	94.57
	2019/07/04–2019/07/10 (Fig. 1c)	126.64
	2019/07/04–2019/07/16	27.26
	2019/07/04–2019/07/22	75.62
	2019/07/04–2019/07/28	89.20
	2019/07/04–2019/08/03	31.32

(see Data and Resources). In addition, we highlight the ability to map small spatial scale (~30 m) fractures having small offsets (>5 mm) using Sentinel-1 data.

Data and Methods

Here, we construct coseismic interferograms using two pre-earthquake acquisitions for each track and all data acquired within a month after the earthquakes (Table 1). Unfortunately, there are no acquisitions between the 36 hr that separated the two events. We produce three types of products using open-source Generic Mapping Tools Synthetic Aperture Radar (GMTSAR) (Sandwell *et al.*, 2016) and Generic Mapping Tools (Wessel *et al.*, 2013) software, with the phase unwrapped using the Statistical-cost, Network-flow Algorithm for Phase Unwrapping software (Chen and Zebker, 2002):

1. The standard interferograms shown in Figure 1 were produced using the nearest acquisitions spanning the earthquakes (Table 1). These were Gaussian filtered at 100 m half-wavelength and sampled at 50 m. Unwrapped and subsampled data, suitable for source modeling, are available on our website. Interestingly, the overall interferometric pattern from this sequence resembles the European Remote Sensing satellites interferogram for the 1999 M_w 7.1 Hector Mine earthquake (Sandwell *et al.*, 2000; Fialko *et al.*, 2002). Both events occurred in similar tectonic context in the ECSZ (Savage *et al.*, 1990), yielding similar moment release and rupturing behavior along the E45S direction.
2. To extract information for smaller scale features, we produce phase-gradient maps directly from the real $R(\mathbf{x})$ and imaginary $I(\mathbf{x})$ parts of the full resolution interferograms (Sandwell and Price, 1998), in which the position vector $\mathbf{x}$ consists of the range r and azimuth a coordinates of the interferogram. Instead of computing the phase gradient from the phase $\phi(\mathbf{x}) = \tan^{-1}(\frac{I}{R})$, which as many 2π discontinuities, one can use the chain rule of differentiation to develop a formula for the phase gradient directly from R and I. The result is $\nabla\phi(\mathbf{x}) = \frac{R\nabla I - I\nabla R}{R^2+I^2}$, in which the gradient operator is $\nabla = (\frac{\partial}{\partial r}, \frac{\partial}{\partial a})$, with r and a denoting the direction of gradient along range (look) and azimuth (flight). The numerical derivative filter must be designed to avoid aliasing short-wavelength noise at the Nyquist wavenumber to longer wavelengths, so we combined a central difference filter with a low-pass Gaussain filter having 0.5 gain at 30 m half-wavelength.
   Phase gradients are very small in the far field of the rupture, so we focus on the second subswath of each TOPS frame and process at full resolution (~15 m). Unlike standard interferograms, these phase gradient maps can be directly stacked without phase unwrapping (Sandwell and Price, 1998). Thus, we applied the same algorithms to every interferogram (Table 1) and averaged them to produce the final phase gradient maps (Fig. 2). The phase gradient maps are essentially strain maps and thus highlight all types of small spatial scale deformation. There are two types of artifacts to consider when interpreting these maps. First, there are artificial linear phase discontinuities at the burst boundaries of the TOPS-mode data. To overcome this, one can estimate the associated azimuthal motion by computing an earthquake source model and include this estimate at the Synthetic Aperture Radar (SAR) coregistration step. Second, the random patterns along the major rupture zones are areas of decorrelation due to extreme ground shaking or deformation rates beyond one radian per pixel.
3. To further define the deformation characteristics of each fracture, we unwrapped the full resolution interferogram following Xu *et al.* (2016), by imposing a coherence mask along the fault and allowing discontinuity in the map. We stacked the unwrapped phase and then high-pass filtered using an 800 m Gaussian filter (Fig. 3). The stacking of unwrapped phase reduces the phase noise to ~1 mm and also reduces atmospheric effect, especially the elevation-dependent component that possess resemblance to deformation pattern. These stacked phase maps are converted to line of sight (LoS) deformation and then decomposed into east–west motion (positive

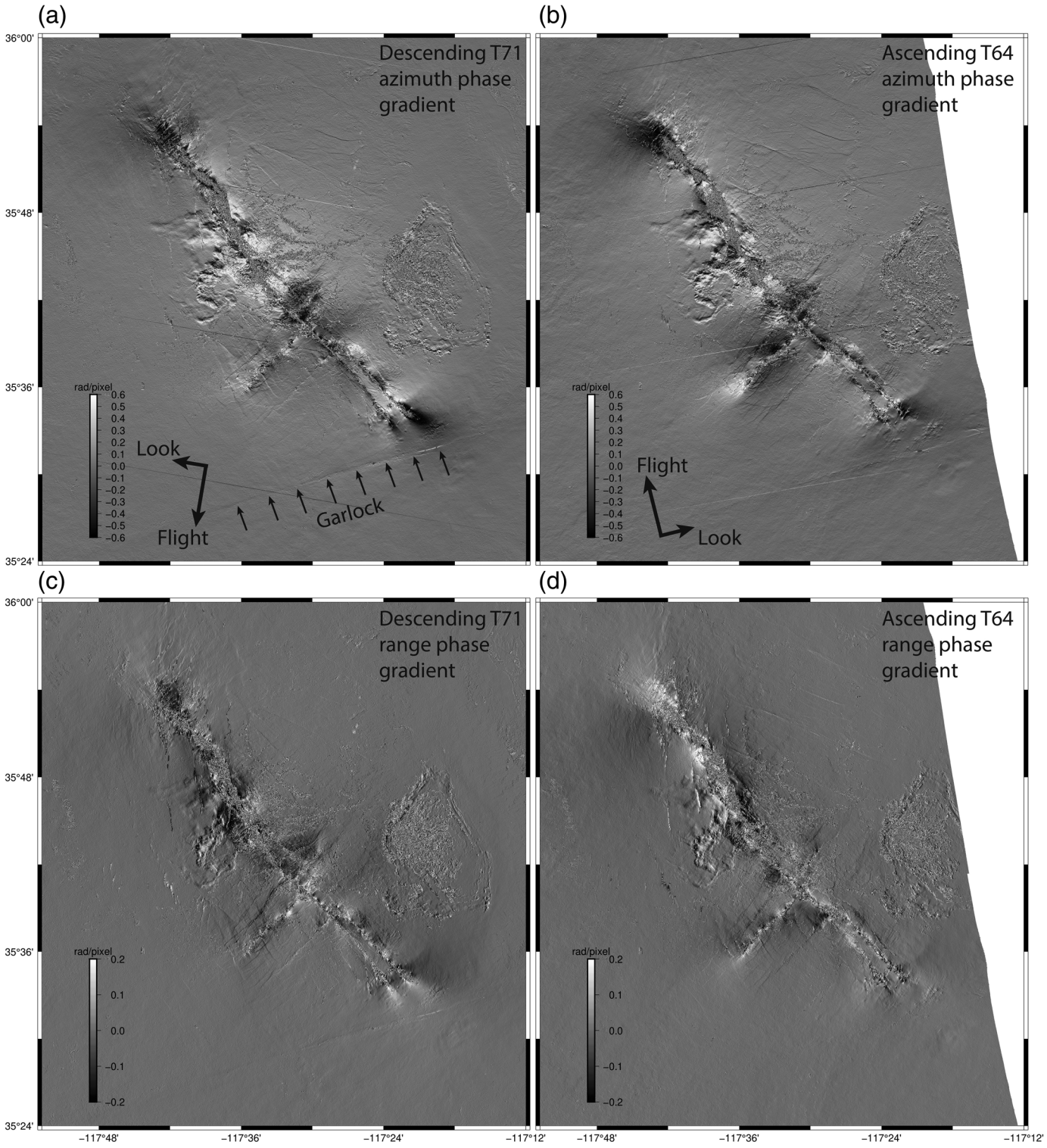

is east) and up–down and south–north (positive is up and south) taking advantage of the satellite look angle for this area being largely the same from the two Sentinel-1 tracks. We then use these decomposed maps to establish the sense of the motion along the fracturing features (e.g., right lateral or left lateral). Deformations as small as 2 mm are well resolved, so one cannot expect to find surface cracks associated with all these linear features.

Figure 2. Stacked phase gradient maps. The gradient is taken along the flight (azimuth) and look (range) direction for both ascending and descending tracks of the Sentinel-1 satellites. (a) The azimuth phase gradient for track T71; (b) the azimuth phase gradient for track T64; (c) the range phase gradient for track T71; (d) the azimuth phase gradient for track T64. Download the kmz/pdf files from the website (see Data and resources) to see much more details.

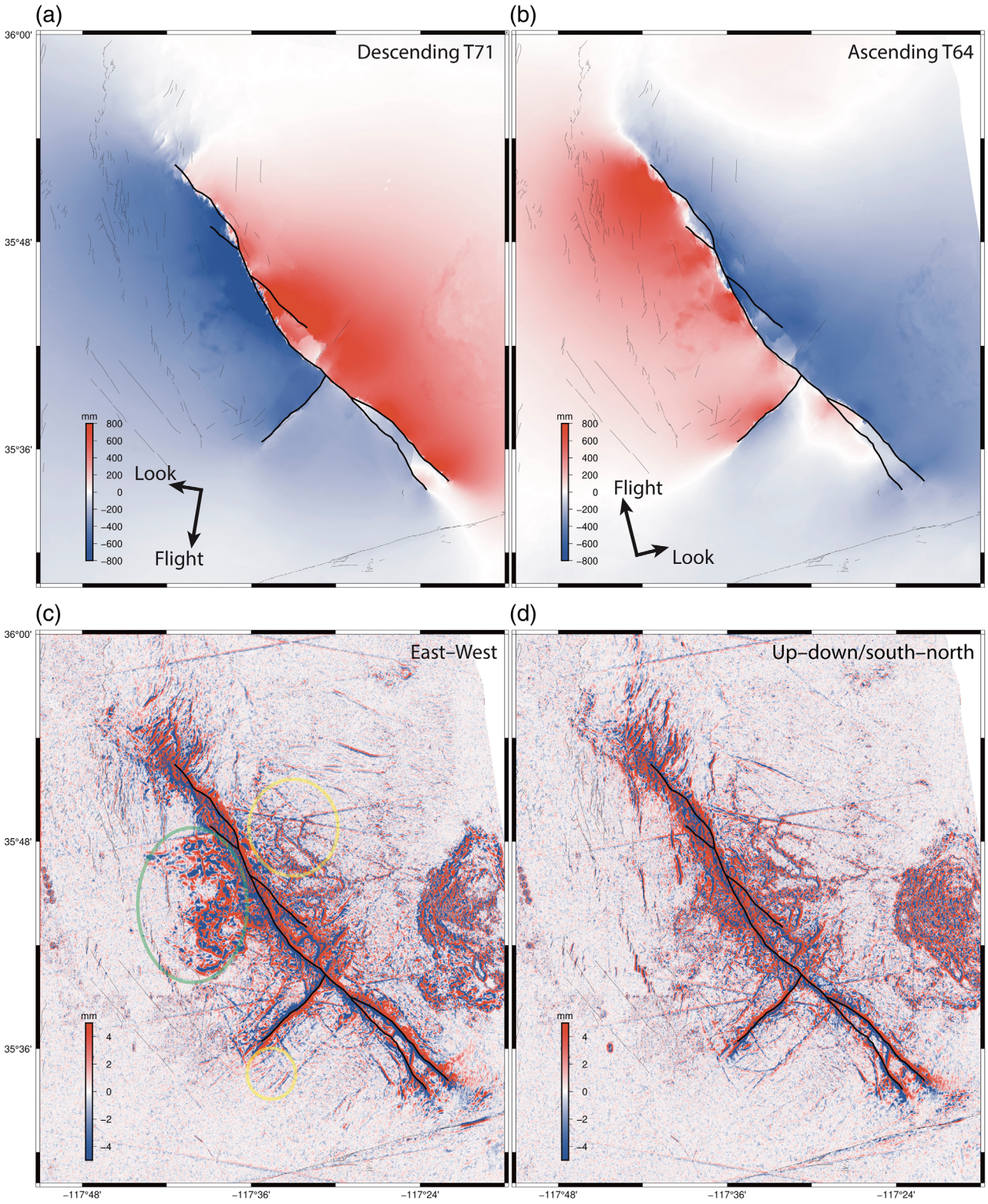

Figure 3. Stacked unwrapped phase and decomposed high-pass filtered stacked unwrapped phase. Stacked unwrapped phase for (a) descending track 71 and (b) descending track 64. For (a) and (b), positive (red) means the ground is moving toward the satellite and negative (blue) means the ground is moving away from the satellite. (c) East–west component of the decomposed high-pass filtered stacked unwrapped phase and (d) up–down and south–north components. For (c), positive (red) indicates motion to the east and negative (blue) indicates motion to the west. For (d), positive indicates motion up or to the south and negative indicates down or to the north. The green oval indicates a region of anomalous east–west dominant deformation. Yellow ovals indicate fractures that have an inferred retrograde sense of slip to the background tectonic stress. The color version of this figure is available only in the electronic edition.

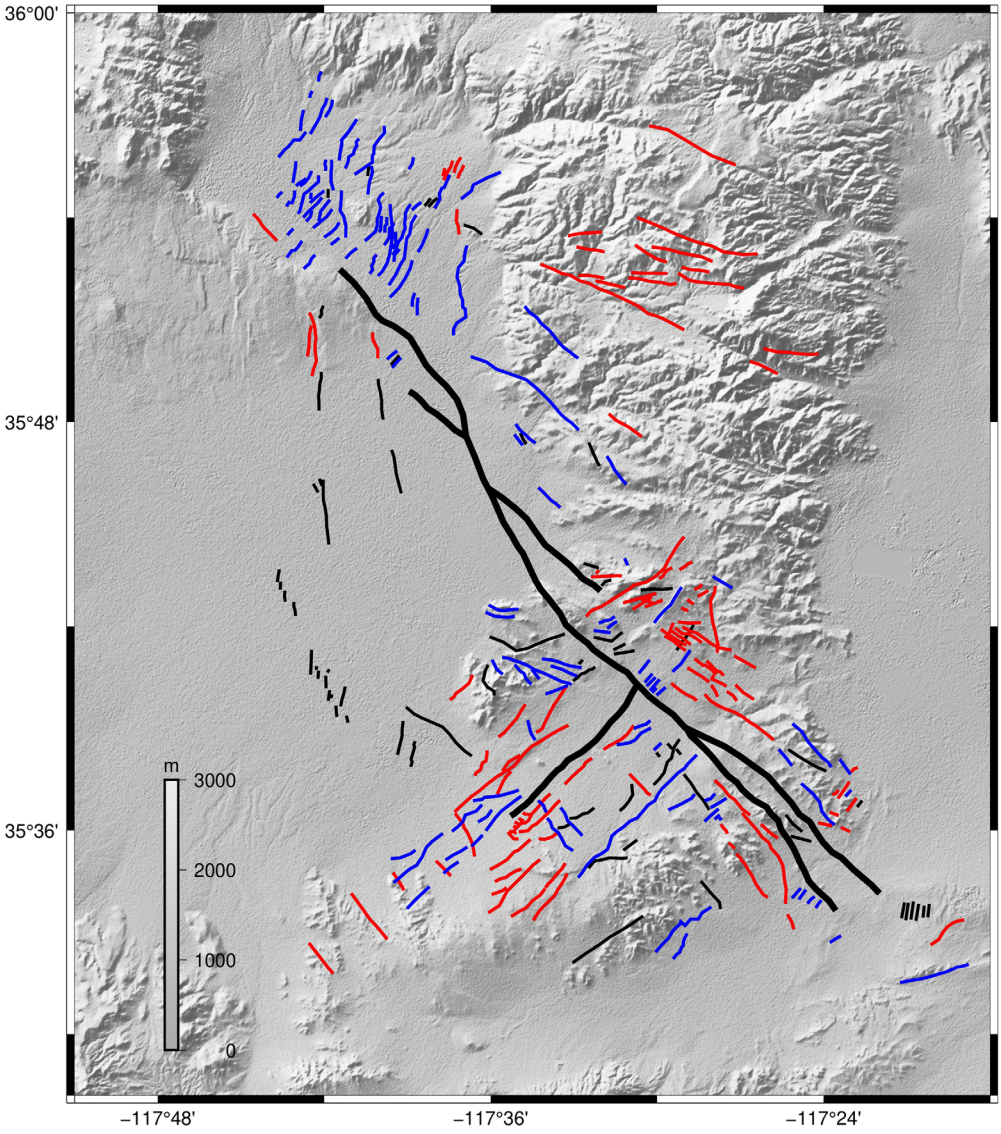

Figure 4. Inferred fracture map from InSAR data around the Ridgecrest earthquake sequence. Black curves denote the main rupture trace as well as the surface fractures that are not predominately strike slip. Red curves are right lateral and blue curves are left lateral. Two areas of retrograde faults are outlined by yellow ovals. The color version of this figure is available only in the electronic edition.

We provide all of the products discussed earlier using an ftp-server-based website (see Data and Resources). The three types of products (1) LoS interferograms, (2) phase gradient maps, and (3) stacked LoS deformation data are provided as geocoded netcdf files as well as kmz format files that can be directly viewed in Google Earth. Specially, the phase gradient maps have been used as an early guide for fault or fracture mapping for field geologists just after the Ridgecrest events. The LoS deformation is further processed to include elevation information and look vectors and put together in ASCII format, ready for use by modelers.

Discussion

The Sentinel-1 Interferometric Synthetic Aperture Radar (InSAR) data shows exquisite detail in the near field of the rupture related to a wide variety of processes. In particular, phase gradient maps revealed a 35 km long left-lateral deformation along the Garlock fault, with the most prominent 3 km section positioned just to the right of the southern end of the M_w 7.1 rupture (Fig. 2). This section has a deformation over 20 mm across the fault within a <500 m wide zone. Other parts of Garlock exhibit much smaller deformation that are difficult to detect using InSAR phase, but are clearly revealed by the phase gradient approach.

Another interesting feature in these maps (Figs. 2 and 3) is the blob-like deformations inside the Naval base west of the M_w 7.1 epicenter (green oval in Fig. 3c). The deformation is east–west dominant, because there is little vertical or north–south signal. This lateral motion is unexpected because there is extensive vertical motion due to liquefaction or surface collapse caused by the nearby rupture. The mechanism of this blob-like, lateral surface motion is unknown to the authors.

The most interesting preliminary finding from this InSAR analysis is the fractures that are inferred to show a sense of slip that is opposite or retrograde to the background tectonic stress. We located the fractures in the high-resolution phase gradient maps and then establish their sense of offset using the east–west component of the high-pass filtered phase. These retrograde fractures occur mainly in two areas (Figs. 3 and 4, yellow ovals). Most of the fractures to the northeast of the M_w 7.1 rupture zone have a right-lateral slip consistent with the background stress. However, there are two prominent fractures, closer to the rupture, having left-lateral slip that is opposite to the tectonic stress but in agreement with the promotion of left-lateral shear on receiver faults of like orientation from preliminary Coulomb stress changes models (see Data and Resources). A second area of retrograde slip is inferred southwest of the M_w 6.4 rupture where we find many fractures having retrograde slip directions. Preliminary Coulomb stress change

models also suggest that these fractures would have left-lateral slip aligned with their strike as a result of the Ridgecrest earthquake sequence (see Data and Resources). Similar retrograde features were also seen in phase gradient maps of the 1999 M_w 7.1 Hector Mine rupture zone (Sandwell *et al.*, 2000) and later interpreted as localized deformation along compliant faults in response to the Coulomb stress change from the earthquake (Fialko *et al.*, 2002). The compliant fault interpretation requires a pre-existing fault zone having 1–2 km wide damage zone. None of the retrograde faults in the Ridgecrest region were mapped previously, so additional field work must be done to identify pre-existing faults.

Conclusions

The Sentinel-1 satellites have the wide swath coverage to monitor large continental earthquakes and also the ability to resolve small-scale deformation. Here, we provide three types of InSAR products to investigate coseismic deformation and strain from the combined M_w 6.4 and 7.1 Ridgecrest earthquakes. The standard LoS deformation maps, also produced by other groups, are generally available for rupture modeling. Our unique analysis of the stacked phase gradient maps reveals hundreds of small fractures and cracks surrounding the main rupture zones probably caused by dynamics and static stress changes. In addition, the stacked and high-pass filtered LoS displacement maps show that several of the fractures have slip directions that are opposite to the background tectonic stress. If these fractures occurred along pre-existing faults, then they could be due to static stress changes associated with damaged (compliant) faults. However, if these fractures were not pre-existing faults or have very sharp phase steps (<400 m wide), then they could be true retrograde slip due to the dynamic or static stresses from the earthquakes. Both possibilities are important for understanding this complex rupture system.

Data and Resources

The Interferometric Synthetic Aperture Radar (InSAR) data used in this article were collected by the Sentinel-1 satellites operated by the European Space Agency (ESA) and are freely available at Sentinel data hub (http://scihub.copernicus.eu/dhus). The corresponding orbit product can be found at Sentinel-1 quality control subsystem (https://qc.sentinel1.eo.esa.int/aux_poeorb/). These products are also archived at Alaska Satellite Facility (ASF, https://vertex.daac.asf.alaska.edu and https://s1qc.asf.alaska.edu/ for data and orbit product, respectively). The seamless Synthetic Aperture Radar (SAR) archive data search and access graphic user interface is provided by UNAVCO (https://web-services.unavco.org/brokered/ssara/gui). Sentinel-1 products are available at https://topex.ucsd.edu/SV_7.1/index.html. All websites were last accessed December 2019.

Acknowledgments

The authors want to thank the European Space Agency (ESA) for their open data policy and thank Alaska Satellite Facility (ASF) and UNAVCO for archiving the data and orbital products. This study was funded by the National Aeronautics and Space Administration (NASA) Earth Surface and Interior Program (NNX16AK93G), the National Science Foundation (NSF) (OAC-1834807), and the Southern California Earthquake Center (SCEC) (18134). SCEC is funded by the NSF Cooperative Agreement EAR-1033462 and the U.S. Geological Survey (USGS) Cooperative Agreement G12AC20038.

References

Chen, C. W., and H. A. Zebker (2002). Phase unwrapping for large SAR interferograms: Statistical segmentation and generalized network models, *IEEE Trans. Geosci. Remote Sens.* **40,** no. 8, 1709–1719.

Fialko, Y., D. Sandwell, D. Agnew, M. Simons, P. Shearer, and B. Minster (2002). Deformation on nearby faults induced by the 1999 Hector Mine earthquake, *Science* **297,** no. 5588, 1858–1862.

Sandwell, D. T., and E. J. Price (1998). Phase gradient approach to stacking interferograms, *J. Geophys. Res.* **103,** no. B12, 30,183–30,204.

Sandwell, D. T., L. Sichoix, D. Agnew, Y. Bock, and J. B. Minster (2000). Near real-time radar interferometry of the Mw 7.1 Hector Mine earthquake, *Geophys. Res. Lett.* **27,** no. 19, 3101–3104.

Sandwell, D. T., X. Xu, R. Mellors, M. Wei, X. Tong, and P. Wessel (2016). *GMTSAR: An InSAR Processing System Based on Generic Mapping Tools*, Second Ed., available at http://topex.ucsd.edu/gmtsar/tar/GMTSAR_2ND_TEX.pdf (last accessed December 2019).

Sansosti, E., P. Berardino, M. Manunta, F. Serafino, and G. Fornaro (2006). Geometrical SAR image registration, *IEEE Trans. Geosci. Remote Sens.* **44,** no. 10, 2861–2870.

Savage, J. C., M. Lisowski, and W. H. Prescott (1990). An apparent shear zone trending north-northwest across the Mojave Desert into Owens Valley, eastern California, *Geophys. Res. Lett.* **17,** no. 12, 2113–2116.

Torres, R., P. Snoeij, D. Geudtner, D. Bibby, M. Davidson, E. Attema, P. Potin, B. Rommen, N. Floury, M. Brown, *et al.* (2012). GMES Sentinel-1 mission, *Remote Sens. Environ.* **120,** 9–24.

U.S. Geological Survey (USGS) (2019a). Event page "M 7.1 - 2019 Ridgecrest earthquake sequence", available at https://earthquake.usgs.gov/earthquakes/eventpage/ci38457511/executive (last accessed December 2019).

U.S. Geological Survey (USGS) (2019b). Event page "M 6.4 - 11 km SW of Searles Valley, CA", available at https://earthquake.usgs.gov/earthquakes/eventpage/ci38443183/executive (last accessed December 2019).

Wessel, P., W. H. Smith, R. Scharroo, J. Luis, and F. Wobbe (2013). Generic mapping tools: Improved version released, *Eos Trans. AGU* **94,** no. 45, 409–410.

Xu, X., D. T. Sandwell, E. Tymofyeyeva, A. González-Ortega, and X. Tong (2017). Tectonic and anthropogenic deformation at the Cerro Prieto geothermal step-over revealed by Sentinel-1A InSAR, *IEEE Trans. Geosci. Remote Sens.* **55,** no. 9, 5284–5292.

Xu, X., X. Tong, D. T. Sandwell, C. W. Milliner, J. F. Dolan, J. Hollingsworth, F. Ayoub, *et al.* (2016). Refining the shallow slip deficit, *Geophys. J. Int.* **204,** no. 3, 1867–1886.

Manuscript received 25 September 2019
Published online 15 January 2020